Supporting Information

MOFs-templated self-polymerization of *p*-phenylenediamine to polymer with hollow box-assembled spherical structure

Chunli Zhou, Ang Li, Dengke Wang, Erzhuang Pan, Xiaohong Chen, Mengqiu Jia*, Huaihe Song*

State Key Laboratory of Chemical Resource Engineering, Beijing Key Laboratory of Electrochemical Process and Technology for Materials, Beijing University of Chemical Technology, 100029, Beijing (China)

Corresponding Author

* Huaihe Song: songhh@mail.buct.edu.cn, Jiamq@mail.buct.edu.cn

Experimental Methods

Chemicals. *P*-phenylenediamine (pPD, 98.5%) was provided by Tianjin Fuchen Chemical Reagent Factory. Cupric nitrate (99.5%) and alcohol were obtained from Beijing Chemical Works and Beijing Tongguang Fine Chemical Company, respectively.

Synthesis of hollow box-assembled poly-pPD spheres. First, 0.76 g of pPD and 1.69 g of $Cu(NO_3)_2 \cdot 3H_2O$ were dissolved in alcohol to form a uniform solution that was subsequently transferred to a Teflon-lined autoclave. A reaction was conducted at 150 °C for 24 h to obtain a precipitate. Hollow box-assembled poly-pPD spheres (HBPSs) with cuprous oxide and Cu particles were obtained after cooling, centrifugation, and drying at 80 °C for 12 h in a vacuum. HBPSs were purified by washing them with ammonium hydroxide for 12 h under a nitrogen atmosphere.

Samples with different reaction times (1 min, 30 min, 1 h, 6 h, and 12 h) were collected to investigate the HBPSs' formation process (labeled as t-product, t = reaction time).

Synthesis of porous hollow box-assembled carbon spheres. Porous hollow box-assembled carbon spheres (PHBCSs) were obtained through the pyrolysis of HBPSs in an N_2 atmosphere (600 °C for 2 h) and the removal of copper nanoparticles by washing with hydrogen peroxide and diluted hydrochloric acid.

Controlled experiment.

Experiment 1: To test the influence of oxygen (in a Teflon-lined autoclave) on the formation of hollow structures, we replaced air with N_2 in a glovebox and repeated the aforementioned solvothermal reaction at 150 °C for 12 h.

Experiment 2: To verify the impact of Cu^{2+} in solution on the formation of hollow boxes, 0.3 g of Cu-pPD was dispersed in alcohol and then transferred to a Teflon-lined autoclave. A solvothermal reaction was conducted at 150 °C for 12 h to obtain the precipitate.

Structural characterization. Scanning electron microscopy (SEM, Zeiss SUPRA 55) and transmission electron microscopy (TEM, Hitachi Ht7700) were conducted to investigate the structural changes of products during the reaction process. The variation in crystal structures from Cu-pPD to poly-pPD was determined through X-ray diffraction (XRD) (Rigaku D/max-2500B2t/PCX system) with Cu Kα radiation (λ = 1.5406 Å) from 5° to 90°. Fourier transform infrared (FTIR, NICOLET-iS50) spectroscopy was used to confirm the composition of products with different reaction times. In situ diffuse reflectance FTIR spectroscopy images and thermogravimetric (TG) curves (Netasch STA 449C) were collected to study the structural changes of Cu-pPD during the pyrolysis process. Moreover, the TG curves of products with different reaction times were recorded to further demonstrate the polymerization process. Specific surface areas and pore size distributions of Cu-pPD, HBPSs, and PHBCSs were obtained using nitrogen sorption tests (ASAP 2020, Micromeritics), which were computed on the basis of the Brunauer-Emmett-Teller (BET) model and Non Local

Density Functional Theory (NLDFT) method assuming the slit-type pore, respectively. The molecular mass of HBPSs was determined through gel permeation chromatography (GPC) to verify the polymerization of pPD. The ^{1}H Nuclear Magnetic Resonance (NMR) spectra were conducted on AV600 in dimethyl sulfoxide (DMSO) to further prove the polymerization. The crystal structure of PHBCSs was observed through high-resolution TEM (HRTEM, JEOL-2100). Defective sites and surface chemical elements of PHBCSs were analyzed using Raman and X-ray photoelectron spectra (XPS) measurements, respectively.

Electrochemical measurements of PHBCSs. First, PHBCSs, acetylene black, and polyvinylidene fluoride were mixed at a weight ratio of 8:1:1 and with a certain volume of N-methyl pyrrolidinone to form a slurry. Subsequently, the slurry was pasted onto a copper foil and dried at 120 °C overnight under a vacuum. Sodium ion batteries (SIBs) were assembled in an argon-filled glove box (Unilab M Braun) by using a CR2025 cell. For the SIB test, metal sodium was used as the negative electrode, glass fiber was used as the separator, and $NaClO_4$ (1 M) in ethylene carbonate and diethyl carbonate at a volume ratio of 1:1 were used as the electrolyte. Cyclic voltammetry measurements were performed at 100 $\mu V\ s^{-1}$ within the range of 0.01–2.8 V on an electrochemical workstation (Zennium, Zahner). Capacity was recorded using a galvanostatic charge/discharge test on a battery testing system (LAND-CT2001A) at various current densities with a voltage window of 0.01–2.8 V.
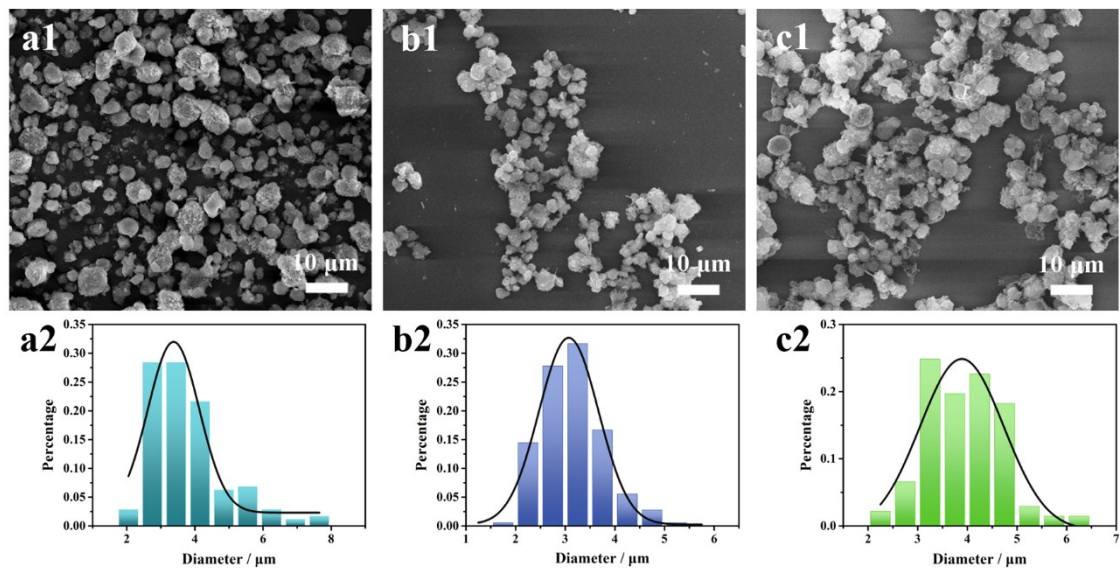
Fig. S1 SEM images of products with different reaction times and the corresponding statistical distribution of the outer diameter: (a) 1 min, (b) 30 min, and (c) 1 h.
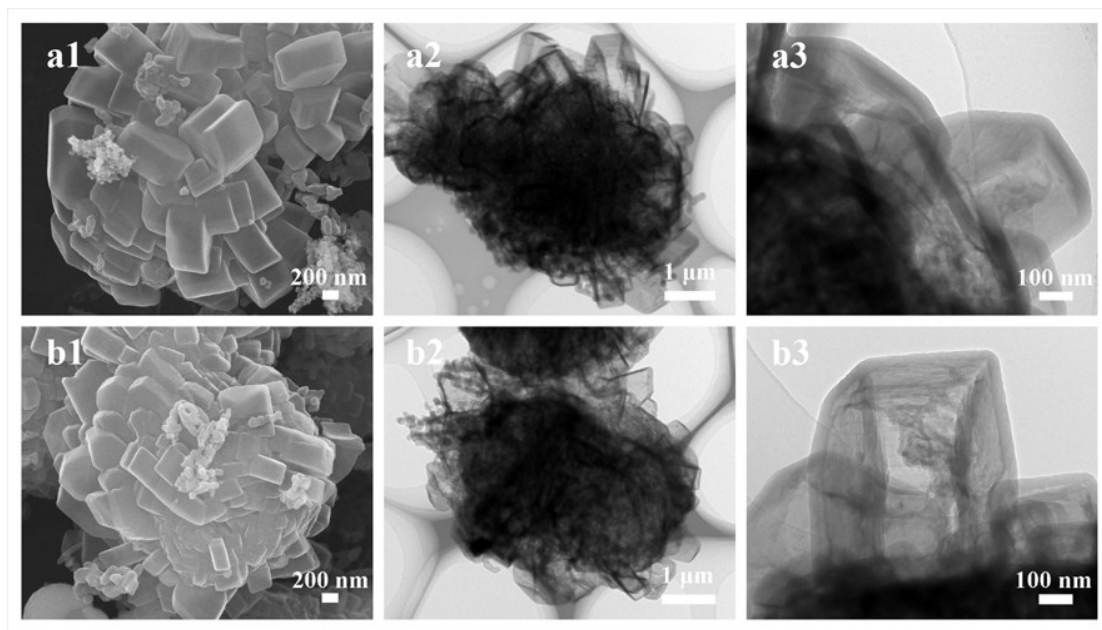

Fig. S2 SEM and TEM images of products with reaction times of (a1–a3) 6 h and (b1–b3) 12 h, respectively.
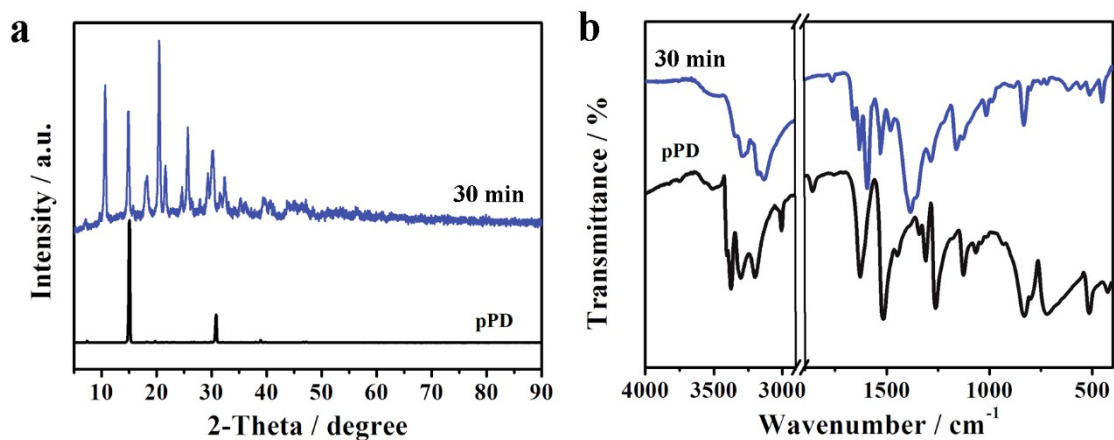
Fig. S3 (a) XRD patterns and (b) FTIR spectra of pPD and the 30 min-product.

In the FTIR spectrum of pPD (Fig. S3b), some absorption peaks at approximately 3300 cm^{-1} could be attributed to the N-H stretching vibration. The strong adsorption peaks at 2957, 1629, and 1516 cm^{-1} represent the presence of benzene rings. Furthermore, the adsorption peak at 830 cm^{-1} could be attributed to an aromatic *p*-disubstituted compound.
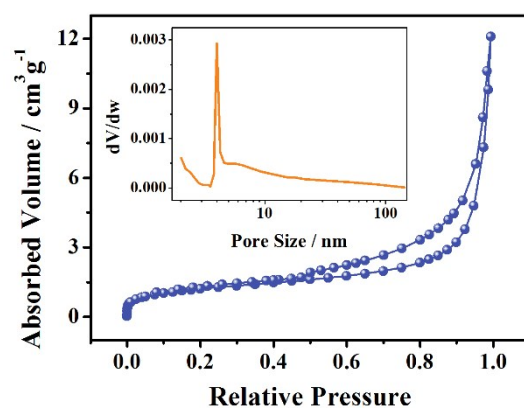

Fig. S4 Nitrogen adsorption–desorption isotherms and pore width distribution of the 30 min-product.
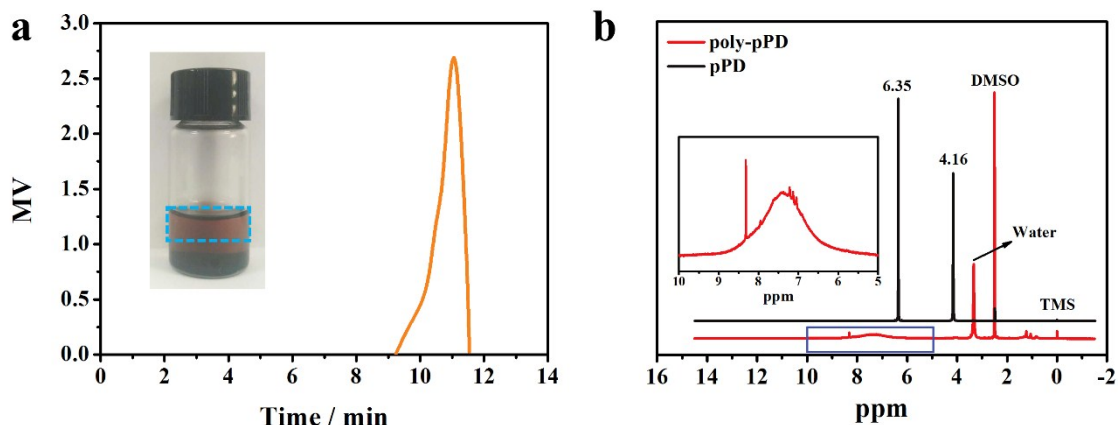
Fig. S5 (a) Gel permeation chromatography traces of HBPSs in tetrahydrofuran, (b) ^{1}H NMR spectra of poly-pPD and pPD.

The molecular weight values of HBPSs is a more direct form of evidence to verify the polymerization of pPD. However, performing these measurements is difficult because of the poor solubility of polyaniline in most organic solvents. As shown in Fig. S5a, most HBPSs powders with high degrees of polymerization cannot dissolve in tetrahydrofuran and sink to the bottom of the bottle. Thus, the supernatant liquid (indicated by the blue rectangle in Fig. S5a) is determined by GPC, which reveals a molecular weight of (M_w) 3726 g mol^{-1}. This value is higher than that of the monomer molecular weight of 108 g mol^{-1} of pPD. This phenomenon clearly confirms the polymerization of pPD.

^{1}H NMR spectra of poly-pPD and pPD were also tested to investigate the structural change after solvothermal reaction. Dimethyl sulfoxide (DMSO) was chosen as solvent because most poly-pPD can dissolve in it. As seen in Fig. S5b, two sharp peaks at 6.35 ppm and 4.16 ppm can be observed in the ^{1}H NMR spectrum of pPD, which can be attributed to the hydrogen atoms on benzene ring and in $-NH_2$, respectively. The two sharp peaks basically disappear in the ^{1}H NMR spectrum of poly-pPD. And a broad peak around 6.5-8.5 ppm and a sharp peak

at 8.32 ppm appear, which would result from aromatic proton resonance of poly-pPD.[1] The formation of broad peak may be from the irregular structure of poly-pPD. Hence, ^{1}H NMR spectra further verify the polymerization of pPD.
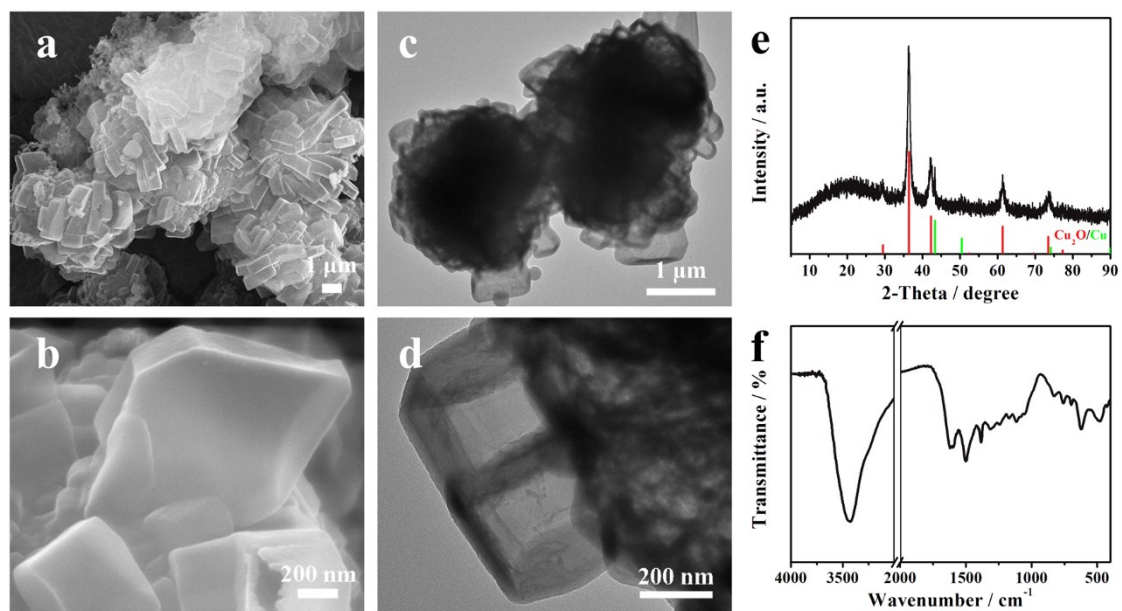

Fig. S6 Structural characterization of the product with a solvothermal reaction under N_2 for 12 h: (a–b) SEM images, (c–d) TEM images, (e) XRD pattern, and (f) FTIR spectrum.
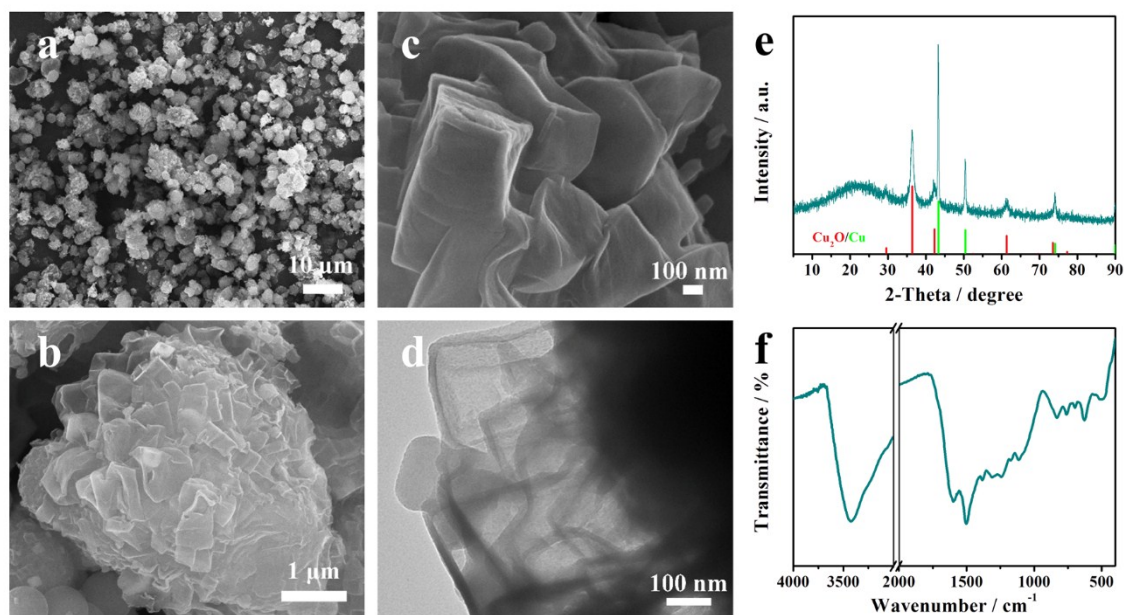
Fig. S7 Structural characterization of the product with solvothermal reaction without Cu^{2+} for 12 h: (a–c) SEM images, (d) TEM image, (e) XRD pattern, and (f) FTIR spectrum.
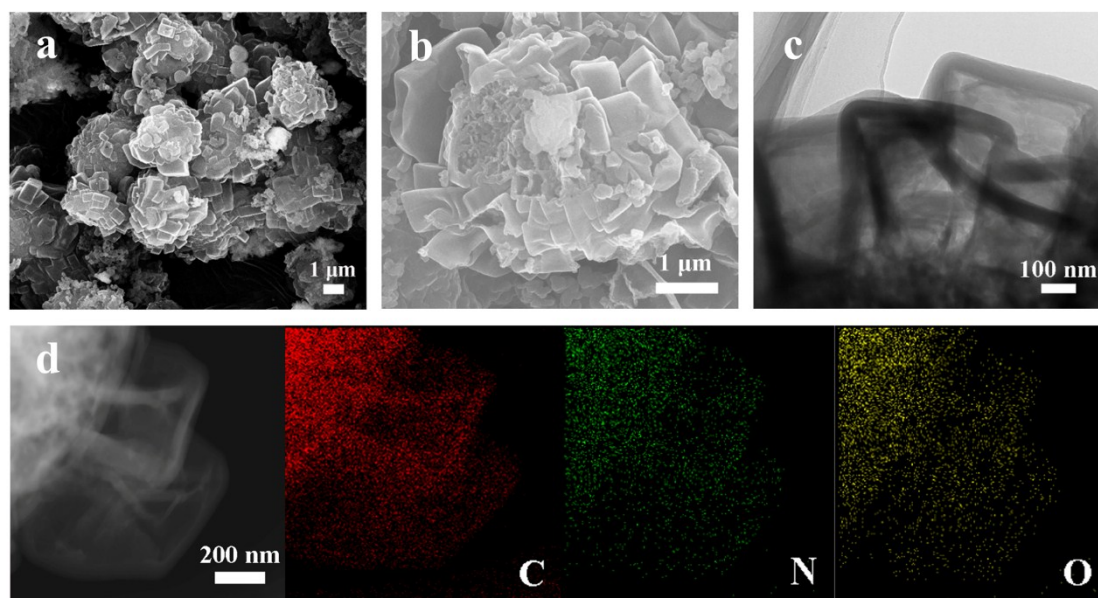

Fig. S8 The structural characterization of HBPSs after washing: (a-b) SEM images, (c) TEM image, (d) High-angle annular dark-field scanning transmission electron microscopy (HAADF-STEM) image with corresponding EDS maps.
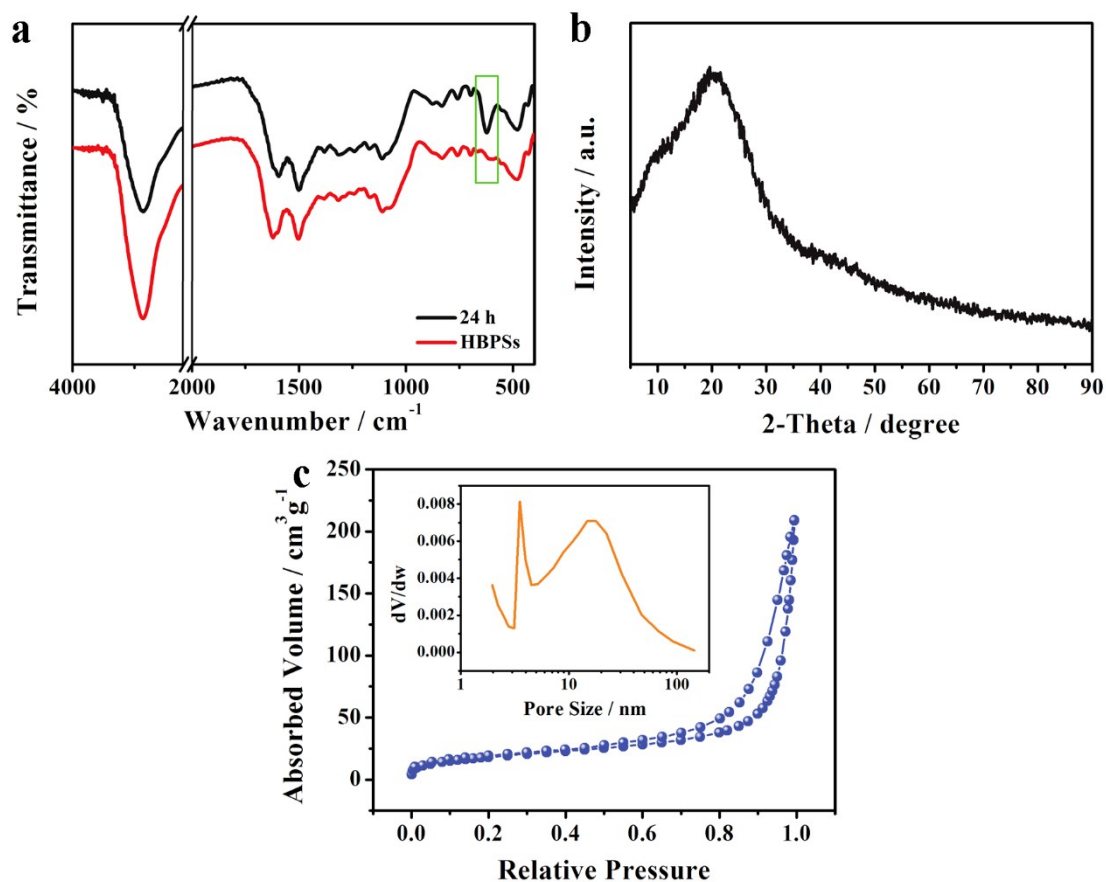
Fig. S9 (a) FTIR spectra of HBPSs before and after washing, (b) XRD pattern, and (c) nitrogen adsorption–desorption isotherms and pore width distribution of pure HBPSs.

As shown in Fig. S9a, the absorption peak at 671 cm^{-1} inside the green rectangle disappears after washing. This peak represents the Cu-O stretching vibration in Cu_2O, suggesting the removal of Cu_2O.
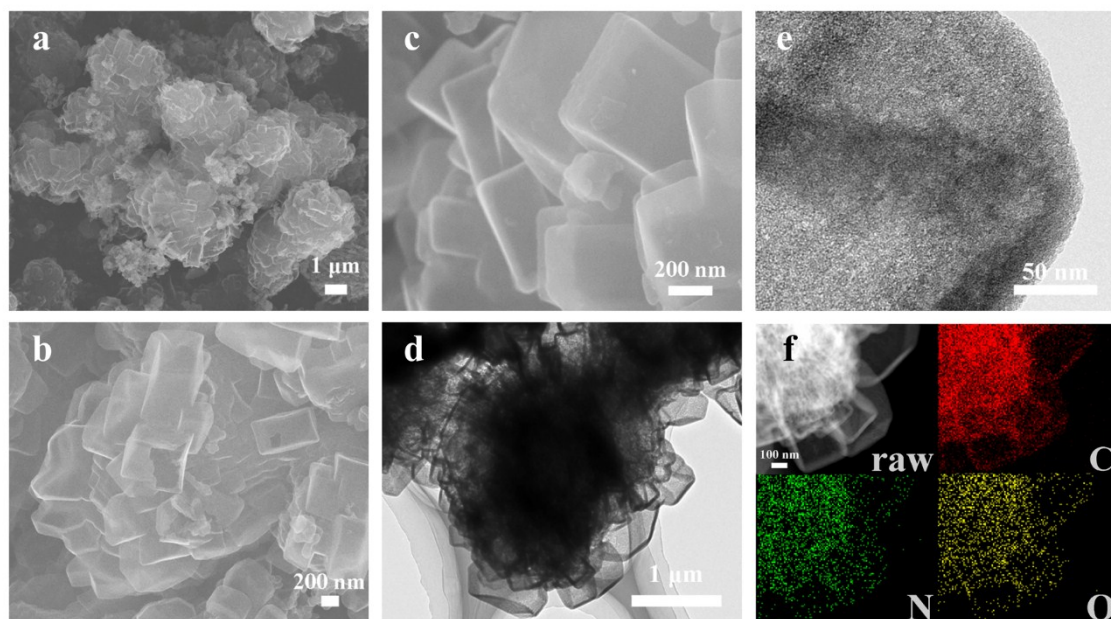
Fig. S10 (a–c) SEM images of PHBCSs, (d–e) TEM images of PHBCSs, and (f) HAADF-STEM image with corresponding elemental mapping of C, N, and O on the PHBCSs, respectively.
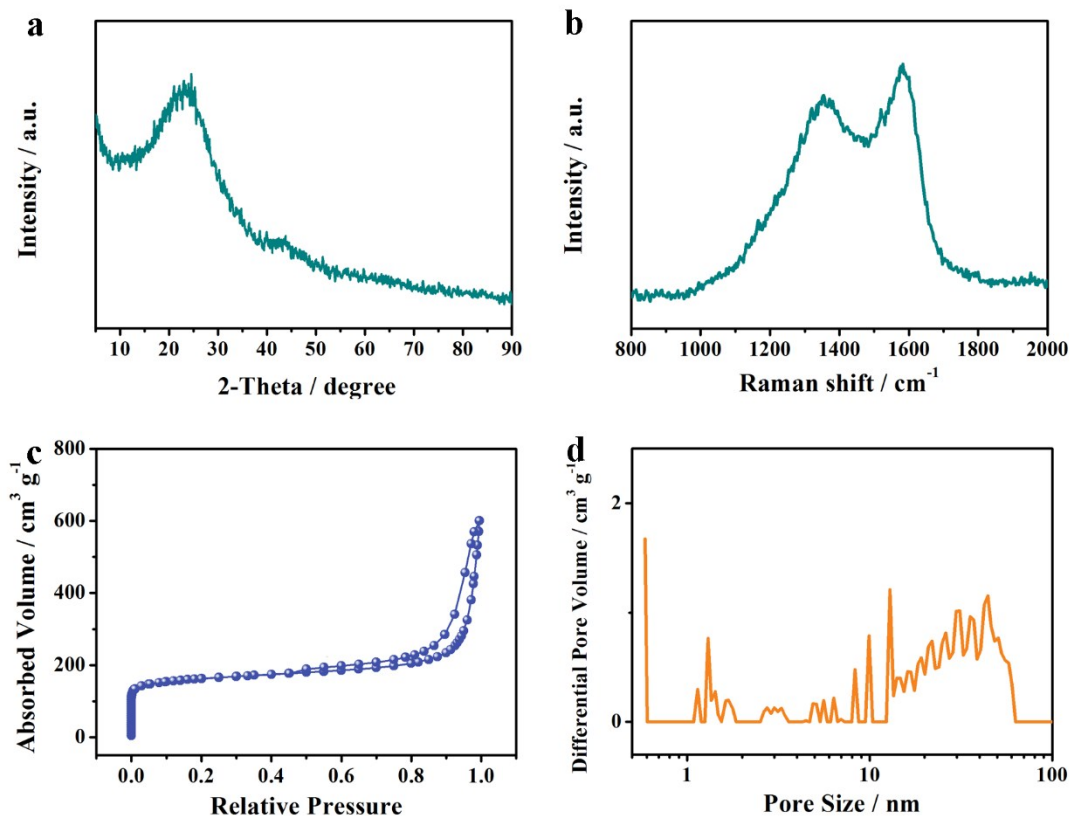
Fig. S11 Structural characterization of PHBCSs: (a) XRD pattern, (b) Raman spectrum, and (c–d) nitrogen adsorption–desorption isotherms and pore width distribution.

As shown in Fig. S11a, the XRD pattern of PHBCSs displays two broad and dispersive diffraction peaks, which can be attributed to the (002) and (100) crystal planes of carbon, respectively, and indicates the amorphous structure of PHBCSs. The Raman spectrum of PHBCSs exhibits a D band (at 1347 cm^{-1}) and G band (at 1586 cm^{-1}), which are associated with disordered/defective carbon and graphitic structures, respectively (Fig. S11b). The I_D/I_G value of PHBCSs is 0.91, suggesting abundant defects and active sites. Nitrogen adsorption–desorption measurements are conducted to determine the pore characteristics of PHBCSs. The isotherms of PHBCSs (as shown in Fig. S11c) are of a mixed type I and IV (a). The rapid rise in the absorbed volume at a low relative pressure and obvious hysteresis loops in the

range of 0.4 to 1.0 suggest that PHBCSs possess some micropores and abundant mesopores. Furthermore, HBCSs possess a high specific surface area (513 m^2 g^{-1}) and a large pore volume (0.93 cm^3 g^{-1}), which can provide more charge transfer channels and effectively promote ion diffusion.
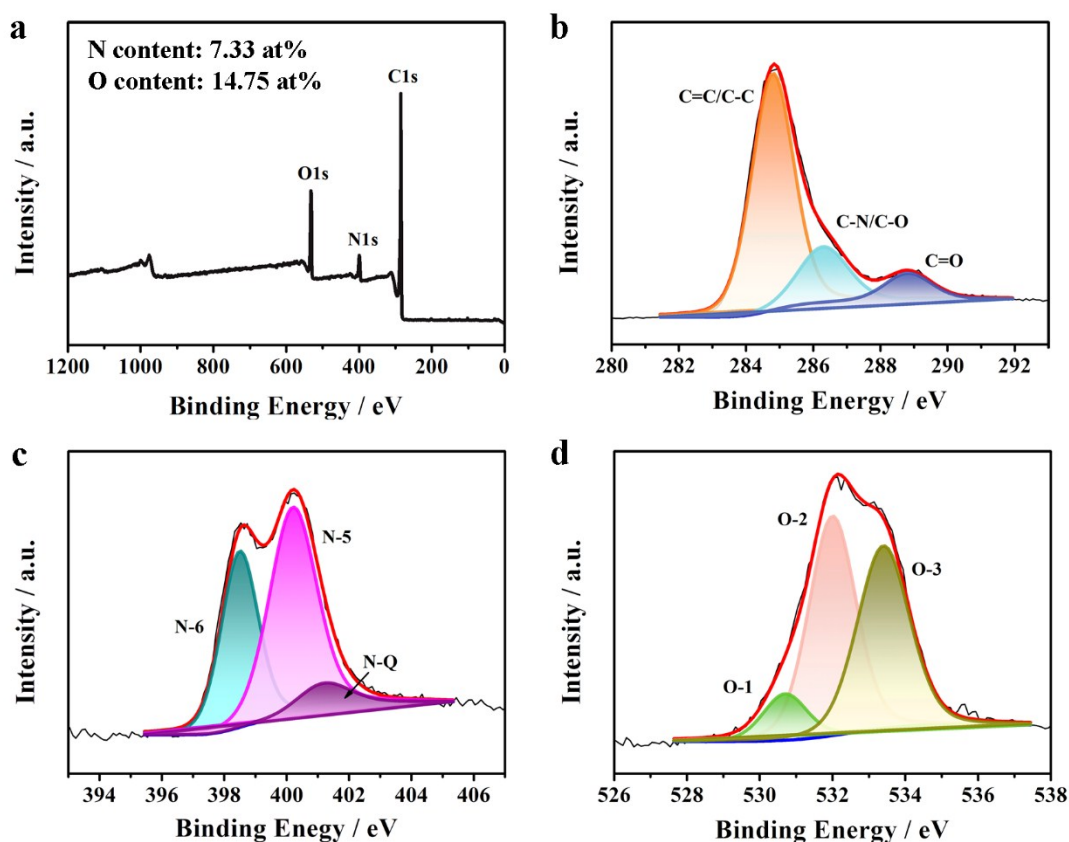

Fig. S12 (a) XPS survey spectra of the PHBCSs; high resolution (b) C 1s, (c) N 1s and (d) O 1s XPS spectra of the PHBCSs.

X-ray photoelectron spectroscopy measurements are implemented to investigate the surface chemical elements of PHBCSs, the results of which are displayed in Fig. S12. Fig. S12a illustrates the coexistence of C, N, and O elements on PHBCSs, illustrating that N, O-codoped carbon materials are prepared through the simple carbonization of HBPSs. The C1s

spectrum of PHBCSs is presented in Fig. S12b, which can be separated into three peaks: C=C/C-C bond (284.8 eV), C-N/C-O bond (286.3 eV), and C=O bond (288.8 eV).[2] N1s is fitted to three peaks: N-6 (pyridinic nitrogen, 398.4 eV), N-5 (pyrrolic nitrogen, 400.0 eV), and N-Q (quaternary-N, 401.3 eV) (Fig. S12c).[3] O1s is also converted to three peaks, namely O-1 (C=O quinone type groups, 530.7 eV), O-2 (C-OH phenol groups and/or C-O-C ether groups, 531.9 eV), and O-3 (chemisorbed oxygen and/or water, 533.4 eV), respectively (Fig. S12d).[4]
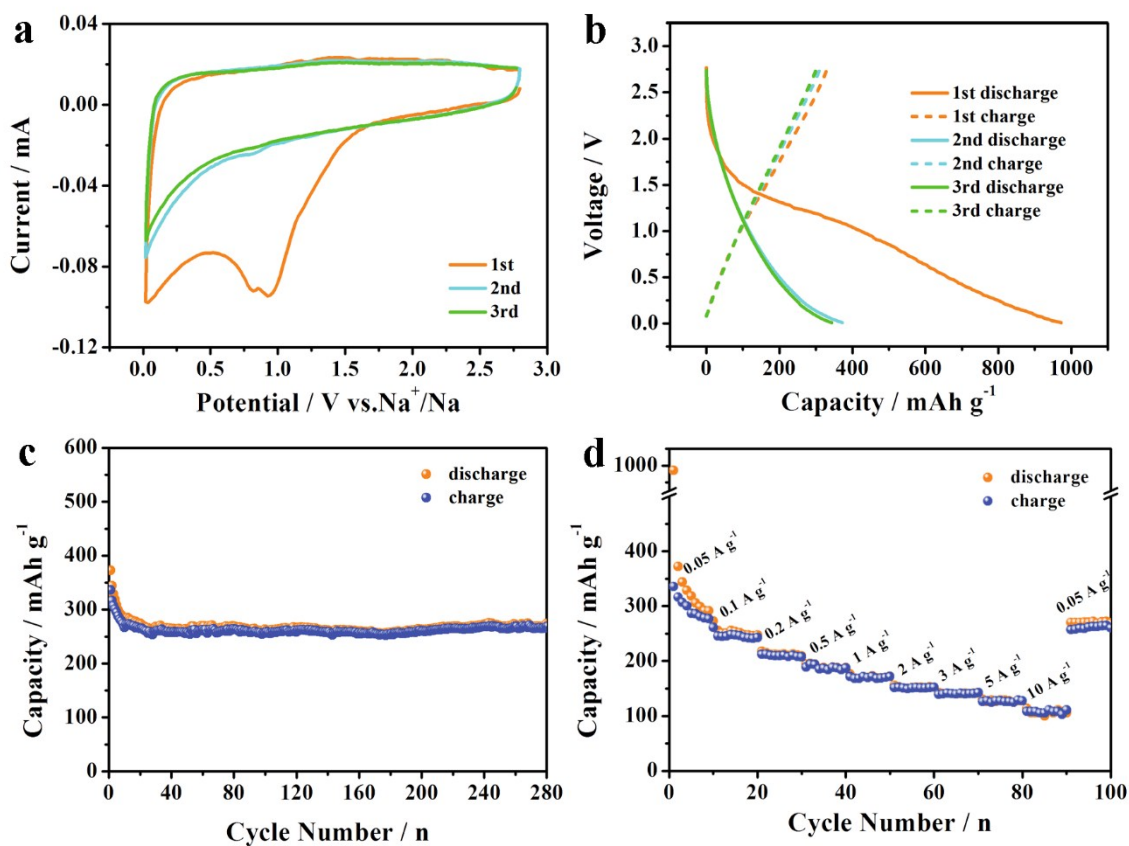

Fig. S13 Sodium storage performance of PHBCSs: (a) cyclic voltammograms, (b) initial three charge–discharge curves at 50 mA g^{-1}, (c) cycle performance at 50 mA g^{-1}, and (d) rate performance from 50 mA g^{-1} to 10 A g^{-1} of PHBCSs as anode materials of sodium ion batteries.

In Fig. S13a, the broad peak that ranges from 1.65 V to 0.85 V can be attributed to the irreversible reaction between sodium ions and surface functional group(s). Another peak at 0.8 V disappearing in the third cycle can be attributed to the formation of a solid electrolyte interface layer on the PHBCSs' surface. Moreover, the sharp cathodic peak near 0.01 V and an anodic peak at approximately 0.2 V represent Na^+ insertion/extraction in PHBCSs. Fig. S13b displays initial three charge–discharge curves at 50 mA g^{-1}; the first discharge curve displays a plateau at approximately 1.0 V, which can be attributed to the formation of the SEI layer. Subsequent cycles only consist of a sloped region, a typical sodiation curve of hard carbons, suggesting that sodium storage in PHBCSs mainly occurs at their surface defect sites.[5]

References
1   (a) S. Mu, *Synthetic Met.*, 2010, **160**, 1931-1937; (b) X. Wang, T. Sun, C. Wang, C. Wang, W. Zhang and Y. Wei, *Macromol. Chem. Phys.*, 2010, **211**, 1814-1819.
2   (a) S. Liu, J. Zhou and H. Song, *Adv. Energy Mater.*, 2018, **1800569**; (b) Y. Dong, S. Zhang, L. Shi, Y. Chen, J. Ma, S. Guo, X. Chen and H. Song, *Mater. Chem. and Phys.*, 2018, **203**, 125-132.
3   (a) H. Lu, R. Chen, Y. Hu, X. Wang, Y. Wang, L. Ma, G. Zhu, T. Chen, Z. Tie, Z. Jin and J. Liu, *Nanoscale*, 2017, **9**, 1972-1977; (b) H. Liu, H. Song, X. Chen, S. Zhang, J. Zhou and Z. Ma, *J. Power Sources*, 2015, **285**, 303-309; (c) F. Hu, J. Wang, S. Hu, L. Li, G. Wang, J. Qiu and X. Jian, *Nanoscale*, 2016, **8**, 16323-16331.
4   (a) C. Zhou, A. Li, B. Cao, X. Chen, M. Jia and H. Song, *J. Electrochem. Soc.*, 2018, **165**, A1447-A1454; (b) D. Hulicova-Jurcakova, M. Seredych, G. Q. Lu and T. J. Bandosz, *Adv. Funct. Mater.*, 2009, **19**, 438-447.
5   (a) C. Bommier, T. W. Surta, M. Dolgos and X. Ji, *Nano letters*, 2015, **15**, 5888-92; (b) Y. Cao, L. Xiao, M. L. Sushko, W. Wang, B. Schwenzer, J. Xiao, Z. Nie, L. V. Saraf, Z. Yang and J. Liu, *Nano letters*, 2012, **12**, 3783-7.